Food Hydrocolloids 152 (2024) 109866

Contents lists available at ScienceDirect

Food Hydrocolloids

journal homepage: www.elsevier.com/locate/foodhyd

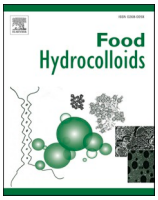

MRI assessment of pH and coagulation during semi-dynamic *in vitro* gastric digestion of milk proteins

Morwarid Mayar [a,b], Mart de Vries [a], Paul Smeets [b], John van Duynhoven [a,*], Camilla Terenzi [a,**]

[a] Laboratory of Biophysics, Wageningen University & Research, Wageningen, the Netherlands
[b] Division of Human Nutrition and Health, Wageningen University & Research, Wageningen, the Netherlands

ARTICLE INFO

Keywords:
Casein
Whey Protein
Heat Treatment
Magnetization Transfer
Chemical Exchange Saturation Transfer
Nuclear Magnetic Resonance

ABSTRACT

Gastric digestion is essential for protein breakdown, which is commonly studied *in vitro*. However, validating *in vitro* models with *in vivo* data is necessary. ^{1}H MRI techniques, including Chemical Exchange Saturation Transfer (CEST) and Magnetization Transfer (MT), are promising for non-invasive assessment of *in vitro* and *in vivo* digestion. We previously demonstrated the ability of these techniques for monitoring *in vitro* milk protein digestion in static conditions. Here, we investigated the performance of CEST and MT for detecting pH and milk protein coagulation in semi-dynamic *in vitro* conditions using whey protein isolate solution (WPIS), low- or high-pasteurized skim milk (LPSM and HPSM, respectively). The asymmetric MT ratio (MTR_{asym}), reflecting the soluble proteins/peptides, decreased with the pH and protein concentration during digestion, with distinct trends observed for the different products. The dual-power CEST method allowed accurate and precise estimation of the pH for WPIS within a pH range of 5–7 on a 7 T NMR spectrometer. *In situ* pH mapping was achieved using a 3 T clinical MRI scanner. The T_2-weighted images, combined with MT ratio (*MTR*) maps, reflecting semi-solid proteins, enabled assessing the coagulum volume and structure during digestion. The *MTR* allowed differentiating the coagulation behaviour of LPSM and HPSM induced by the heat treatment. In conclusion, CEST and MT can be used to monitor milk protein digestion, and the effect of milk heat treatment in semi-dynamic gastric conditions. Future work will investigate the feasibility of these techniques for *in vivo* gastric milk protein digestion studies.

1. Introduction

Proteins are essential nutrients, and their nutritional benefits rely on how well they are digested in the gastro-intestinal tract. Gastric digestion plays a crucial role in breaking down proteins, and it involves de- and re-structuring of foods to facilitate further breakdown in the intestinal tract (Mackie et al., 2020). Cow's milk is an important source of high-quality proteins in the human diet (Tome, 2012). The digestion of milk proteins (MP), namely casein and whey, starts in the gastric phase, during which acid- and pepsin-induced aggregation of casein micelles leads to the formation of a semi-solid coagulum. Intact whey proteins (WPs) remain mostly in solution or form small aggregates (Huppertz & Chia, 2021). Heat treatment is a common procedure in milk processing, and may lead to changes in protein structure, thereby affecting gastric protein digestion (van Lieshout et al., 2019). The effect of heat treatment on protein digestion has been studied using static (Tunick et al., 2016) or (semi-)dynamic *in vitro* digestion models (Mulet-Cabero et al., 2019; Wang et al., 2018) that simulate human gastro-intestinal digestion.

Static *in vitro* digestion models (Brodkorb et al., 2019; Ménard et al., 2018) are useful because they are simple, well controlled, and can provide insights into the digestion kinetics and chemical composition of the digesta. However, static models do not fully mimic the complexity of the digestive tract, because they do not incorporate gastric secretion, emptying and motility as well as hormonal responses. In comparison to static *in vitro* digestion models, dynamic models are physiologically more realistic: they include gastric secretion, emptying and motility, and the stomach shape is taken into consideration (Dupont & Mackie, 2015; Mackie et al., 2020). However, such models are highly complex, time-consuming and more expensive than static models. Therefore, semi-dynamic *in vitro* models have been developed, in which gastric secretion and emptying are mimicked by inflow of gastric juice and removal of gastric content (Deng et al., 2022; Mulet-Cabero et al., 2020).

* Corresponding author.
** Corresponding author.
E-mail addresses: john.vanduynhoven@wur.nl (J. van Duynhoven), camilla.terenzi@wur.nl (C. Terenzi).

https://doi.org/10.1016/j.foodhyd.2024.109866
Received 27 September 2023; Received in revised form 29 January 2024; Accepted 5 February 2024
Available online 10 February 2024

The gastric compartment in these models is simply a glass beaker kept at 37 °C, and mixing is achieved either by using an overhead stirrer or by flow of air bubbles. However, data from these models need to be verified with *in vivo* data on intra-gastric digestion from humans. Such data can, in turn, be used to improve *in vitro* digestion models. However, the conventional methods used to analyze *in vitro* digestion samples, including measurements of pH, coagulum weight, protein content, and degree of hydrolysis cannot be directly utilized *in vivo* because they require invasive sampling of digesta. Consequently, these methods become impractical for *in vivo* studies and raise ethical concerns. Therefore, non-invasive methods that can be used to study both *in vitro* and *in vivo* digestion in humans need to be developed.

Magnetic Resonance Imaging (MRI) holds great potential for studying *in vivo* protein digestion in humans because it can be used to non-invasively acquire detailed images of the chyme inside the gastrointestinal tract (Smeets et al., 2020). For such applications, MRI has been mainly used to assess macroscopic gastric processes, such as gastric emptying and phase separation *in vivo* (Spiller & Marciani, 2019). However, the anatomical images used in these studies do not provide a quantitative and molecular-scale measurement of gastric protein digestion, which is crucial for monitoring gastric MP structuring and breakdown over time, for studying the effect of heat treatment on gastric digestion, and for comparing *in vitro* and *in vivo* data.

Previous studies have demonstrated that the transverse Nuclear Magnetic Resonance (NMR) relaxation time (T_2) of water can be used to monitor the digestion of WP gels in static (Deng et al., 2020) or semi-dynamic (Deng et al., 2022) *in vitro* gastric digestion models, as well as *in vivo* (Deng et al., 2023). T_2 MRI mapping, combined with fat quantification, has recently been utilized to assess semi-dynamic *in vitro* digestion of a meal containing bread and cheese (Musse et al., 2023). These studies have proven that T_2 measurements via spin-echo-based MRI methods are useful for observing digestion-mediated changes in the transverse relaxation time of water via chemical exchange with proteins or self-diffusional averaging (Hills et al., 1989). However, such measurements cannot be used to directly detect semi-solid macromolecular protons with short T_2-values of <100 μs (Hinrichs et al., 2007; Mayar et al., 2022), due to the long dead times, typically around few ms, of clinical MRI scanners. Although the T_2 of water is sensitive to macromolecular dynamics through chemical exchange with proteins and/or diffusional averaging, quantifying exchange rates and macromolecular proton fractions requires, e.g., measurements of T_2-values at different echo times to obtain T_2-dispersion curves (Carver & Richards, 1972). While such measurements have been used for characterizing food systems in a laboratory setting (Gottwald et al., 2005; Hills et al., 1990), applying these methods *in vivo* is challenging due to the long measurement times of T_2-dispersion experiments. Specific MRI techniques have been developed for detecting short- T_2 components, including Ultra-short Echo Time (UTE) and Zero Echo Time (ZTE) MRI. However, these techniques are typically restricted to measuring T_2 values larger than 300 μs, which are much longer than those of immobile coagulated proteins. Moreover, these measurements require hardware that is not readily available on most clinical MRI scanners (Weiger & Pruessmann, 2019). In addition, aforementioned T_2 MRI measurements lack the sensitivity to detect low-abundant proteins and peptides, such as in milk with a relatively low protein content of around 3.4%, which is further diluted during digestion.

Saturation Transfer MRI techniques, Magnetization Transfer (MT) and Chemical Exchange Saturation Transfer (CEST) (Ward et al., 2000; Wolff & Balaban, 1989) offer several advantages over T_2-mapping: MT and CEST can be used to indirectly detect semi-solid or low-abundant solute (macro)molecules through their interaction with water. Moreover, these techniques are already widely applied in clinical human research and do not require specialized hardware. Additionally, semi-quantitative parameters, namely the MT ratio (*MTR*) and the asymmetric *MTR* (MTR_{asym}), can be measured rapidly within 1.3 min (Mayar et al., 2023). In MT and CEST measurements, a radio-frequency (RF) pulse is employed to selectively saturate the magnetization of the semi-solid and/or low-abundant solute protons of interest. The saturated magnetization is subsequently transferred to the mobile water protons, resulting in a reduction of the detected water signal intensity. The saturation transfer processes in MT and CEST measurements are predominantly driven by ^{1}H dipolar coupling and chemical exchange, respectively (Balaban & Ceckler, 1992; van Zijl et al., 2018; Zhou et al., 2023).

The *MTR* parameter can provide insights into the mobility and content of (semi-)rigid macromolecules (Henkelman et al., 2001). Clinical applications of MT MRI have demonstrated the ability of the latter to detect even subtle alterations in semi-solid tissues, e.g. in terms of macromolecular content or structural integrity (Van Obberghen et al., 2018; Welsch et al., 2008).

CEST MRI is designed to measure the chemical exchange of labile protons between specific solute molecules, including proteins and peptides, and bulk water. The MTR_{asym} parameter obtained from CEST measurements is a measure of ^{1}H chemical exchange, and is sensitive to changes in solute concentration and pH (Wu et al., 2016). CEST MRI has gained increasing recognition as a non-invasive technique for *in vivo* pH mapping (Chen et al., 2017; Tang et al., 2020; Wu et al., 2015). Various processes that are essential for gastric protein digestion, such as gastric emptying, and MP coagulation and hydrolysis, depend on pH. Gastric pH evolves over time, due to gastric juice secretion, gastric emptying and the buffering capacity of the proteins.

In addition to pH evolutions, gastric digestion involves alterations in protein/peptide concentration, and modifications in the state of proteins, including coagulation, solubilization, and hydrolysis (Huppertz & Chia, 2021; Mulet-Cabero et al., 2020). As such, MT and CEST MRI are highly promising for assessing these concomitant changes during *in vitro* and *in vivo* gastric protein digestion. Accordingly, we have previously demonstrated that MT and CEST MRI can be used to detect protein hydrolysis and gastric breakdown of the MP coagulum in a static *in vitro* digestion model (Mayar et al., 2022, 2023). The next step is to apply these techniques for MP digestion under more complex dynamic digestion conditions, including gastric secretion and emptying. Therefore, the aim of this work was to investigate the potential of CEST and MT MRI for monitoring pH and MP coagulation in semi-dynamic *in vitro* gastric digestion conditions. A WP isolate (WPI) solution (WPIS), low pasteurized skim milk (LPSM) and high pasteurized skim milk (HPSM) were used as test products to evaluate the sensitivity of CEST and MT for gastric MP digestion, and the effect of heat treatment on the digestion. The MRI measurements were carried out in the laboratory using a 7 T vertical bore NMR spectrometer, and inside a 3 T clinical MRI scanner. The 7 T vertical bore NMR spectrometer allows for high flexibility in setting values of acquisition parameters, and was therefore used for developing and testing of the methods. Although more limited in the range of accessible acquisition parameter values, the 3 T clinical scanner enables *in situ* measurements of the semi-dynamic digestion model, and was therefore utilized to evaluate the feasibility of future *in vivo* studies.

2. Materials and methods

2.1. Materials

Commercially available WPI (87 wt% protein, 0.5 wt% fat, 2 wt% carbohydrates, and 0.5 wt% salt) was purchased from Bulk™ (Essex, UK). Commercially available LPSM (3.6 wt% protein, 0.1 wt% fat, 4.7 wt % carbohydrates and 0.13 wt% salt) was purchased from a grocery store (The Netherlands). Pepsin (631 activity units/mg), calcium chloride hexahydrate, hydrochloric acid, L-serine, potassium chloride, sodium bicarbonate, sodium chloride, sodium hydroxide, Rhodamin B, and tri tris(hydroxymethyl)-aminomethane hydrochloride were purchased from Sigma Aldrich (St. Louis, USA). Pepstatin A and Pierce™ BCA Protein Assay Kit were purchased from ThermoFischer Scientific (Massachusetts, USA). Milli-Q water (resistivity 18.2 MΩ cm at 25 °C, Merck

Millipore, USA) was used in all experiments.

2.2. Preparation of WPI solutions and HPSM

WPI powder was dissolved in Milli-Q water at different concentrations and stirred at room temperature for 1 h. The pH of the solutions was adjusted to pH values ranging between 3 and 7 using 0.1 M sodium hydroxide (NaOH), and 0.1 and 1 M hydrochloric acid (HCl). The protein solutions were stored at 5 °C and were used within one day. The WPIS were prepared and measured in duplicate. HPSM was prepared from a commercially available LPSM, with a WP denaturation level of 3% by heating the latter in a water bath for 30 min after reaching a temperature of 80 °C, resulting in a WP denaturation level 0f 90% (data not shown).

2.3. Preparation simulated gastric fluid

The simulated gastric fluid (SGF) composition was based on the INFOGEST protocol (Brodkorb et al., 2019) and was prepared at pH 2. To determine the volume of HCl required to lower the pH during digestion, SGF (pH 2) and the WPIS or SM were mixed in a 50:50 ratio in a test tube. Slow titration with 1 M HCl was performed until pH 2 was reached, and the required volume of HCl was noted as an indicator of the amount of 1 M HCl to be added to the SGF for gastric secretion as suggested by Mulet-Cabero et al. (2020). Pepsin was added to the SGF at an activity of 4000 U/mL to ensure a pepsin activity of 2000 U/mL when mixed with the WPIS or SM at a 50:50 meal to SGF ratio.

2.4. Semi-dynamic in vitro gastric digestion

Semi-dynamic *in vitro* gastric digestion was conducted using an MRI-compatible semi-dynamic digestion model established by Deng et al. (2022). The set-up has several components, including a syringe pump to simulate gastric secretion (NE-500 Programmable OEM Syringe Pump, New Era Pump Systems, Inc., USA), a water-jacketed beaker acting as the stomach chamber, and a circulating water bath (Julabo GmbH, Germany) to maintain the temperature at 37 °C. Mixing was performed manually because magnetic stir bars are not MRI-compatible, and the previously described method of mixing with air bubbles (Deng et al., 2022) was impractical due to foaming of the WPIS and SM. Stirring was performed using a stirring rod right before the MRI acquisition. The digestion conditions were based on the standardized semi-dynamic *in vitro* digestion parameters reflecting adult digestion (Mulet-Cabero et al., 2020). To initiate digestion, 200 mL of pre-heated 12% WPIS, LPSM or HPSM at 37 °C was placed in the beaker containing 20 mL of pre-heated SGF at 37 °C. The gastric secretion was started with a rate of 2 mL/min. The gastric emptying rate was based on the caloric content of the food and was 4 or 4.3 mL/min for 12% WPIS or SM, respectively. Gastric emptying was performed manually by removing gastric content every 10 min using a 50 mL syringe with a tip that had an inner diameter of ~2 mm, simulating the emptying of food particles through the pylorus (Bornhorst & Paul Singh, 2014). The activity of pepsin in the removed gastric content was inhibited by adding 400 μL of a 0.72 μM Pepstatin A solution and the samples were stored in the freezer at −20 °C. CEST measurements on these samples were conducted on the 7 T NMR spectrometer, and the pH and protein concentration values were measured as well. For the *in situ* MRI measurements at 3 T, gastric content was removed after each set of MRI acquisitions for each digestion time to mimic gastric emptying.

2.5. 7 T MRI measurements

^{1}H CEST MRI measurements of WPIS and gastric content samples were conducted at room temperature (RT) in a vertical bore magnet with a magnetic field strength of 7 T, corresponding to a ^{1}H frequency of 300.13 MHz. The spectrometer comprised an Avance NEO console (Bruker Biospin, Fallanden, Switzerland) and was equipped with a Micro 2.5 RF coil with an inner diameter of 30 mm and a Micro 2.5 micro-imaging gradient system. To enable simultaneous measurements of multiple samples, 2 mL of WPIS or gastric content samples was transferred to a 10 mm NMR tube, and three of these tubes were placed inside a larger 25 mm tube. An additional 5 mm NMR tube containing a glucose solution was included as a reference tube. The sample tubes were surrounded by an aqueous solution containing 5 mM sodium chloride and 10 mM copper sulphate. Measurements were conducted using a Rapid Acquisition with Relaxation Enhancement (RARE) sequence combined with the saturation transfer module in Paravision 360. The saturation pulse consisted of a train of 10 block pulses (BP) with a pulse length (t_p) of 100 ms and an inter-pulse delay (t_{delay}) of 10 μs, resulting in a saturation time (T_{sat}) of 1 s. The B_1 amplitude was set to 1.5 or 3 μT. To obtain ^{1}H CEST spectra, saturated images, with signal intensity S_{sat}, (Equation (1) in 2.8) were acquired using 67 frequency offset (Δ) values equally spaced from −10 to 10 ppm, resulting in a CEST spectral resolution of 0.3 ppm. In addition, a reference image without saturation, with signal intensity S_0, was acquired (Equation (1) in 2.8). Water Saturation Shift Referencing (WASSR) (Kim et al., 2009) spectra were measured to construct a B_0-map for B_0-inhomogeneity correction of the CEST spectra. For the WASSR measurement, B_1 of 0.2 μT and T_{sat} of 50 ms were used. WASSR spectra were measured using 31 Δ values ranging between −1.5 and 1.5 ppm with a spectral resolution of 0.1 ppm. The imaging parameters for both CEST and WASSR measurements were: in-plane field-of-view (FOV) of 30 mm × 30 mm and respective resolution of 0.23 × 0.23 mm for three axial slices with thickness of 2 mm and interslice gap of 1 mm. Sinc3 RF pulses were used for excitation and refocusing with a flip angle of 90° and 180°, respectively. A repetition time (TR) of 5 s, a turbo factor (TF) of 32, and an effective echo time (TE_{eff}) of 78 ms were used, resulting in a total measurement time of 21 min and of 11 min for the CEST and WASSR measurements, respectively.

2.6. 3 T MRI measurements

For *in situ* monitoring of digestion, the stomach chamber of the semi-dynamic model was placed inside a 3 T clinical MRI scanner (Philips Ingenia Elition X, Philips Medical Systems, the Netherlands). A 16-channel small extremity coil was wrapped around the stomach chamber. MRI scans were performed at baseline (before addition of the WPIS or SM), at t = 0 min (right after addition) and every 10 min until t = 60 min or 80 min for WPIS or SM, respectively. During each scan, both the gastric secretion and circulating water bath were switched off to avoid artifacts caused by motion and influx of SGF. For each digestion time CEST and WASSR data, a T_2-weighted image and a B_1-map were acquired. For both CEST and WASSR measurements, an S_0 reference image (Eq. (1) in 2.8) at Δ = 450 ppm was acquired. For CEST measurements, S_{sat} images (Eq. (1) in 2.8) were acquired at Δ = -2.7, 2.7 and 10 ppm with a T_{sat} of 1 s and a B_1 of 1.5 and 3 μT. WASSR spectra were acquired using 21 Δ-values ranging from −1.5 to 1.5 ppm, with a T_{sat} of 0.05 s and a B_1 of 0.2 μT. CEST and WASSR measurements were conducted using a RF saturation pulse combined with a RARE sequence for pH mapping experiments. Five axial slices were acquired in an interleaved manner with a FOV of 120 mm × 120 mm, in-plane resolution of 0.94 mm × 0.94 mm, slice thickness of 3.5 mm and no inter-slice gap. SINC pulses were used for excitation and refocusing with an excitation flip angle of 90° and the first refocusing flip angle was 180° followed by 110° pulses. A TR of 3.2 s, TF of 38, and TE_{eff} of 80 ms were used, resulting in a total measurement time of 98.6 s and 44.6 s for B_1 = 1.5 and 3 μT, respectively. The WASSR spectra were acquired using the same imaging parameters as described above, yielding a measurement time of 164 s.

MTR maps of the coagulum were obtained using an RF saturation pulse combined with a Gradient Recalled Echo (GRE) sequence to acquire 33 axial slices with a slice thickness of 3.5 mm and no inter-slice gap, which allowed coverage of the whole gastric content. The FOV

and in-plane resolution were the same as for the RARE measurements described above. A SINC excitation pulse with a flip angle of 7°, *TR* of 4.4 ms, *TE* of 2.1 ms, and *TF* of 252 were used, resulting in a measurement time of 68.3 s and 71.4 s for a B_1 of 1.5 μT and 3 μT, respectively.

The RARE sequence was adopted to acquire 33 T_2-weighted axial slices with a slice thickness of 3.5 mm and no inter-slice gap to allow coverage of the whole gastric content. The other parameters were the same as for the RARE measurements described above but with a *TR* of 1 s, and a *TF* of 43, with total measurement time of 26 s. The B_1 map was acquired using the dual refocusing echo acquisition mode (DREAM) sequence (Nehrke & Börnert, 2012) with a *TR* of 11 ms, *TE* of 3.32 and 6.55 ms, and *TF* of 136, and the total measurement time was 26.1 s.

2.7. Protein concentration measurements

The total protein concentration in the supernatant of the gastric content samples was estimated by the Bicinchoninic Acid (BCA) method with the use of Pierce™ BCA Protein Assay Kit. The pH of the samples was adjusted to pH 7 using 0.1 or 1 M NaOH and the samples were centrifuged for 15 min at 4000 *g*. The supernatant was collected and diluted 100× and 30× for the WPIS and SM samples, respectively. The calibration curve consisted of 25, 125, 250, 500, 750 and 1000 μg/mL bovine serum albumin (BSA) standard solutions. For the measurement, 25 μL of standard solution, sample or blank was pipetted in duplicate in a different well of a clear bottom 96-wells well-plate (Greiner Bio-One, the Netherlands). To this 200 μL of BCA reagent was added, the plate was mixed for 30 s using a well-plate mixer and incubated at 37 °C for 30 min. After cooling down to room temperature, the absorbance was measured at 562 nm using microplate reader (Spectramax M2, USA).

2.8. MRI data processing and analysis

All processing and calculations were done in MATLAB R2019b (MathWorks, Massachusetts, USA). A WASSR B_0 map was constructed and used for voxel-wise B_0-inhomogeneity correction of the 7 T CEST spectra as previously described (Mayar et al., 2023). Region-of-Interest (ROI) masks of the middle slice of the sample tube were drawn manually, and the mean signal intensity within the ROI was used to construct the CEST spectra, where S_{sat}/S_0 is plotted as a function of Δ. The MTR_{asym} was calculated according to Eq. (1).

$$MTR_{asym} = (S_{sat}(-\Delta) - S_{sat}(+\Delta))/S_0 \quad \text{Eq. 1}$$

The MTR_{asym} area was calculated as the area under the curve (AUC) between 1.2 and 4 ppm. To evaluate CEST MRI for pH mapping, the dual-power CEST method was used (Longo et al., 2014). This method involves measuring CEST at two B_1 amplitudes to calculate the Ratio of RF Power Mismatch (*RPM*). The CEST effect and, consequently, the MTR_{asym} depend on several factors, including the solute concentration, the chemical exchange rate (k_{ex}), which in turn is linked to pH, the longitudinal relaxation rate of water (R_1^w) and the saturation efficiency (α). We note that k_{ex} is also affected by temperature, which was therefore kept constant during the measurements. Moreover, the WPIS was brought to a temperature of 37 °C before the start of the digestion experiment for the *in situ* measurements on the 3 T clinical MRI scanner. The α value can be approximated by $\alpha \approx (\gamma B_1)^2/((\gamma B_1)^2 + {k_{ex}}^2)$, where γ is the gyromagnetic ratio of ^{1}H in $rad{\cdot}s^{-1}{\cdot}T^{-1}$. By calculating the ratio of the MTR_{asym} at two B_1 values (Eq. (2)), it is possible to compensate for the concomitant changes in both concentration and R_1^w, which makes the *RPM* solely dependent on k_{ex} and, hence, pH. The *RPM* value was calculated for amine protons (Δ = 2.7 ppm) using a B_1 combination of 1.5/3 μT. Linear calibration lines for the acid- and base-catalysed chemical exchange regimes were constructed by taking the logarithm of the *RPM* and were used to predict the pH of the validation and digestion samples.

$$RPM = \frac{\left[(1 - MTR_{asym})/MTR_{asym}\right]_{1.5\mu T}}{\left[(1 - MTR_{asym})/MTR_{asym}\right]_{3\mu T}} \quad \text{Eq. 2}$$

The different stages of the processing and analysis of the data acquired at 3 T is outlined in Fig. 1. First, the MTR_{asym} per voxel was calculated according to Eq. (1), and was used to construct MTR_{asym} maps of the gastric content (Fig. 1; top). Next, a WASSR B_0 map was constructed in the same way as done for the 7 T data. However, a CEST spectrum could not be acquired during the *in situ* measurements at 3 T due to their long measurement time. Instead the MTR_{asym} was acquired using Δ = ± 2.7 ppm, and voxel-wise correction of MTR_{asym} values was performed using the regression-based fast B_0-inhomogeneity correction method (Sun, 2020). In brief, the B_0- inhomogeneity artifact was estimated using the polynomial function shown in Eq. (3).

$$MTR_{asym}(x,y) = A + \left[C_1 \cdot \delta B_0(x,y) + C_2 \cdot \delta B_0^2(x,y)\right] \quad \text{Eq. 3}$$

Here *A* is the dimensionless composite parameter, namely $(f_s \cdot k_{sw})/R_1^w$, in which f_s is the fraction of solute protons, k_{sw} is the solute-water ^{1}H chemical exchange rate and R_1^w is the longitudinal relaxation rate of the bulk water pool. C_1 and C_2 are coefficients (in seconds squared) determined from the polynomial fitting, and δB_0 is the B_0 shift in Hz per voxel. The B_0-inhomogeneity effect on direct RF saturation, also called spillover, and saturation efficiency is described by the first- and second-order terms, respectively. The MTR_{asym} was voxel-wise corrected for B_0-inhomogeneity by subtracting the B_0 artifact, $C_1 \cdot \delta B_0(x,y) + C_2 \cdot \delta B_0^2(x,y)$ from the MTR_{asym}. The B_0-corrected MTR_{asym} values obtained at a B_1 of 1.5 and 3 μT were corrected for B_1-inhomogeneity using the two-point contrast–B_1-correction described by Windschuh et al. (2015). The resulting B_0- and B_1-corrected MTR_{asym} maps were used to calculate the *RPM* values for each voxel, which were subsequently used to determine the pH per voxel using the acid- or base-catalysed chemical exchange calibration lines.

For characterizing the MP coagulation and breakdown (Fig. 1; bottom), coagulum MRI masks were obtained by intensity thresholding of the T_2-weighted images using the multithresh function (Otsu's method) with one level in MATLAB. This thresholding method allowed for the identification of low-intensity imaging voxels corresponding to the coagulum. Using the coagulum MRI mask, the volume of the coagulum was calculated by multiplying the voxel volume by the total number of coagulum voxels. Such imaging mask was also applied to the S_{sat} and S_0 images in order to construct the *MTR* maps of the coagulum at Δ = 10 ppm (Eq. (4)) and calculate the mean *MTR* value for the coagulum voxels at each digestion time point.

$$MTR = 1 - (S_{sat}/S_0) \quad \text{Eq. 4}$$

2.9. Storage and loss modulus measurements

The storage (*G'*) and loss (*G"*) modulus of the coagulum were measured at t = 20, 40 and 70 min of semi-dynamic digestion. For each rheological measurement, carried out in duplicate, the coagulum was removed from the beaker and any excess liquid was discarded. A 25 mm circular sample was cut out from the centre of the coagulum. The samples were stored at 5 °C until 30 min before the measurements, after which they were kept at room temperature. Measurements were performed using an Anton Paar Rheometer (MCR 302, Anton Paar, Germany) equipped with a sandblasted parallel plate geometry. The development of G' and G'' was monitored at a frequency of 1 Hz and strain of 0.1–10%. The coagulum samples were measured within 2.5 h after their preparation.

2.10. Confocal laser scanning microscopy (CLSM)

The microstructure of the coagulum was studied using a Rescan

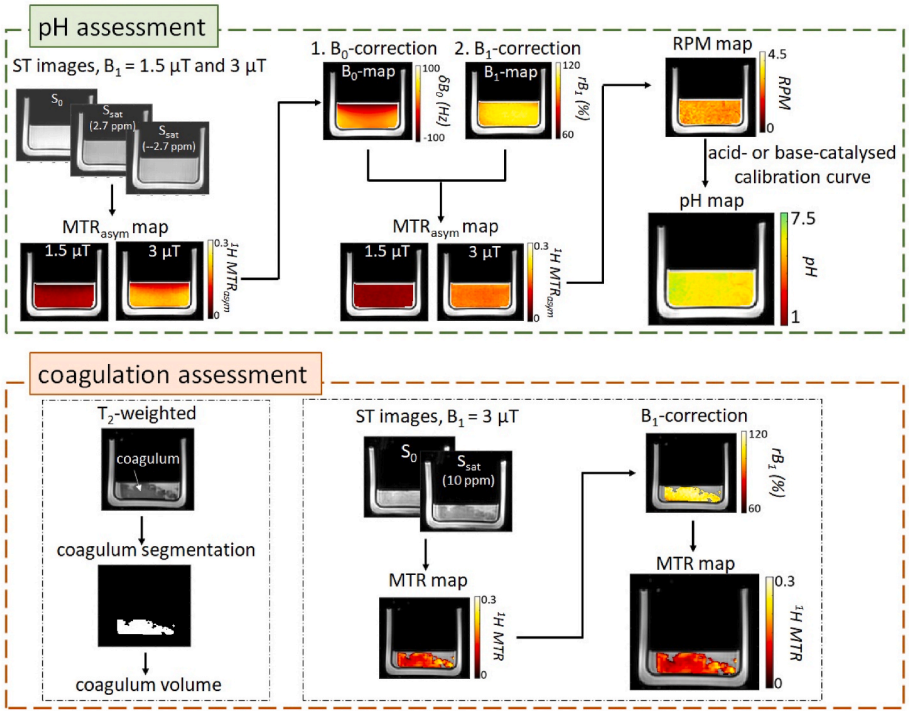

Fig. 1. Schematic outline of the different stages of the processing and analysis of data acquired on the 3 T clinical MRI scanner for the assessment of pH (top) and coagulation (bottom) during semi-dynamic gastric digestion.

Confocal Microscope (RCM) (Confocal.nl, The Netherlands). Rhodamine B (fluorescent dye) was used to stain proteins with an excitation line at 561 nm. The coagulum was collected after 20, 40 and 70 min of digestion, and a small piece of approximately 10 mm × 5 mm was cut from the centre of the coagulum. The samples were stained with 1% (w/v) of Rhodamine B for 5 min, placed on a glass microscope slide and examined with a 63× water immersion objective lens. Images were recorded using MicroManager 2.0.

2.11. Statistical analysis

All statistical analysis was performed in MATLAB 2019b. The error bars in the figures represent the standard deviation (SD). In the case of duplicate experiments, the pooled SD over the time or pH series was calculated (Eq. (5)) and reported in the figure captions. This calculation relies on the assumption that the variances over the measurement series are homoscedastic. This assumption holds true for our data since no systematic trends in the variances were observed.

$$S_{pooled} = \sqrt{\frac{\sum_{i}^{k} S_i^2}{\sum_{i}^{k} n_i - k}} \quad \text{Eq. 5}$$

where S_i^2 is the variance for each measurement point (time or pH), n is the number of samples per measurement point ($n = 2$) and k is the total number of measurement points.

The normalized root mean square deviation (*NRMSD*) (Eq. (6)) was used to evaluate the agreement between the pH values estimated using the CEST MRI approach and those measured with a pH electrode.

$$NRMSD = \frac{1}{\overline{y^m}} \sqrt{\frac{\sum_{i=1}^{n} \left(y_i^m - y_i^e\right)^2}{n}} \quad \text{Eq. 6}$$

where $\overline{y^m}$ is the mean of the pH values measured by a pH electrode; y_i^m are the pH values measured by a pH electrode for each measurement point i; y_i^e are the pH values estimated using the CEST MRI approach for each measurement point i; n is the total number of measurement points.

The uncertainty in the pH estimated with the acid- or base-catalysed calibration curves was estimated using Eq. (7).

$$S_{pH} = \frac{S_y}{|m|} \sqrt{\frac{1}{k} + \frac{1}{n} + \frac{\left(\overline{y}_{sample} - \overline{y}_{std}\right)^2}{m^2 \sum_{i=1}^{n} (x_i - \overline{x})^2}} \quad \text{Eq. 7}$$

where S_{pH} is the SD in the estimated pH, S_y is the standard error in the y-estimate of the calibration curve, m is the slope of the calibration curve, k is the number of replicate measurements of the sample, n is the number of calibration points, $\overline{y}_{sample}$ is the average response of the sample, $\overline{y}_{std}$ is the average response of the calibration standards, x_i is the pH of the individual calibration standards, and $\overline{x}$ is the average pH of the calibration standards. The 95% confidence interval (CI) in the estimated pH was determined as $pH \pm t \bullet S_{pH}$, where t is the critical t-value for $\alpha = 0.05$ and $df =$ n-2.

3. Results and discussion

3.1. In vitro gastric digestion of WPIS, LPSM and HPSM

For 12% WPIS, a transition from a homogeneous solution to a system with small insoluble particles was found to start around 30 min based on visual observation, which coincided with reaching a pH of 4.5 (Fig. S1), close to the iso-electric point (pI) of α-lactalbumin (4.2) and β-lactoglobulin (5.1), causing both proteins to aggregate and form a precipitate (Nicolai et al., 2011; Pederson et al., 2006). These small insoluble aggregates are difficult to observe in the top-view photographs (Fig. 2a), but can be discerned at t = 60 min. They were removed from the stomach chamber with the syringe used to mimic gastric emptying due to their size of less than 2 mm (the inner diameter of the syringe tip). For LPSM and HPSM, coagulation was observed at t ≥ 10 min and t ≥ 20 min, respectively (Fig. 2a). Based on visual inspection, the coagulum of LPSM appeared compact and became smaller in volume as digestion progressed, while for HPSM a softer and looser coagulum was formed.

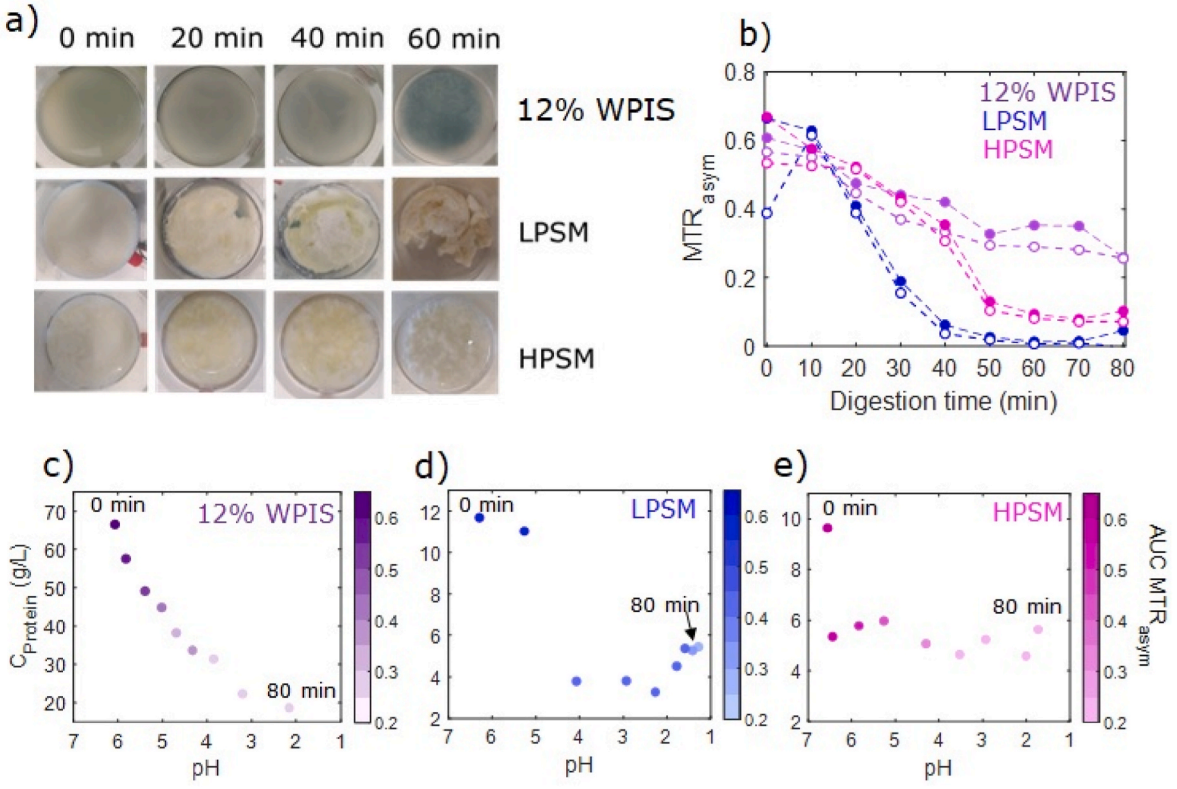

Fig. 2. *For 12% WPIS, LPSM and HPSM: (a) Photographs from the top of the stomach chamber at increasing digestion time from left to right; (b) evolution of the AUC* MTR_{asym} *for the gastric content samples during semi-dynamic in vitro digestion measured on a* 7 T NMR *spectrometer. The filled and empty symbols represent repeats of the same experiment. The pooled SD over the time series was 0.04, 0.07 and 0.04, respectively, for WPIS, LPSM and HPSM. 2D scatter plots for (c) 12% WPIS, (d) LPSM and (e) HPSM showing the AUC* MTR_{asym} *as a function of* pH *and protein concentration during semi-dynamic in vitro gastric digestion. The* pH *axis is inverted to follow the digestion time. The colour of the datapoints is weighted by the AUC* MTR_{asym} value. *The values represent the mean of the duplicate experiments, and the individual datasets can be found in* Fig. S1. *The pooled SD for the* pH *and concentration was 0.07 and 6.5, 0.3 and 0.4, 0.2 and 1.3, respectively, for WPIS, LPSM and HPSM.*

The consistency of the coagulum depends on the extent of WP denaturation, as denatured WPs can form s-s bridges with κ-casein, resulting in WP-casein aggregates. The formation of these aggregates results in a softer and looser MP coagulum during gastric digestion (Ye et al., 2019), which explains the observed difference in the consistency of the MP coagulum between LPSM and HPSM. In the case of LPSM, only the supernatant was removed by gastric emptying starting from t = 20 min, while for HPSM, small and soft coagulated proteins were removed until the end of digestion.

The area under the MTR_{asym} curve (AUC MTR_{asym}) of the gastric content samples, obtained from the ^{1}H CEST spectra, is shown in Fig. 1b. During 80 min of digestion, the AUC MTR_{asym} decreased by 90%, 80% and 50% for LPSM, HPSM and 12% WPIS, respectively. The MTR_{asym} is influenced by changes in protein concentration and pH, as described previously (Mayar et al., 2023). Both protein concentration and pH (Fig. S1) decreased during semi-dynamic digestion due to the removal of soluble or small aggregated proteins, and due to the secretion of acidic SGF. The 2D scatter plots in Fig. 2c–e shows that the AUC MTR_{asym} decreased in accordance with the decrease in protein concentration and pH observed during digestion.

For 12% WPIS, protein concentration and pH continuously decreased, resulting in a continuous decrease in the AUC MTR_{asym}. In the case of LPSM and HPSM, the protein concentration decreased from t = 0–20 min, followed by small fluctuations until 80 min. These fluctuations may be attributed to proteins and polypeptides being released from the coagulum into the liquid phase as digestion progressed. A similar trend was reported for the semi-dynamic gastric digestion of MP powder (Mulet-Cabero et al., 2020). Whereas the start and end pH were similar for all test products, the variations during digestion were different. The pH decreased rapidly for LPSM, while for HPSM the decrease was slower and the pH remained higher throughout the digestion. The trend observed for HPSM was more similar to that of 12% WPIS, particularly in the first 40 min of digestion. This difference can be attributed to the difference in coagulation behaviour between the differently heated milk products. In the case of LPSM, the majority of the caseins were incorporated into the coagulum, resulting in a liquid phase with a low amount of proteins and, hence, limited buffering capacity. This resulted in a more rapid decrease in pH, and, hence, AUC MTR_{asym}. On the other hand, HPSM did not exhibit a clear phase separation, leading to a higher buffering capacity in the liquid phase and a slower decrease in pH, similar to WPI. Overall, these results demonstrate that the MTR_{asym} reflects variations in pH and protein concentration that occur during semi-dynamic digestion, and it is sensitive to differences in gastric digestion among products with different protein composition and heat treatment.

3.2. CEST MRI pH mapping of gastric digestion

In the previous section, we found that the MTR_{asym} followed the variations in pH that occur during gastric digestion. Therefore, we further explored the use of CEST MRI for pH mapping under gastric digestion conditions. First, a validation was performed using standard WPIS and gastric content samples using the 7 T NMR spectrometer, followed by a proof-of-concept experiment for *in situ* pH mapping during semi-dynamic *in vitro* gastric digestion on a 3 T clinical MRI scanner.

3.2.1. Validation of CEST MRI for pH mapping at 7 T

The MTR_{asym} curves showed a clear dependence on the B_1 amplitude

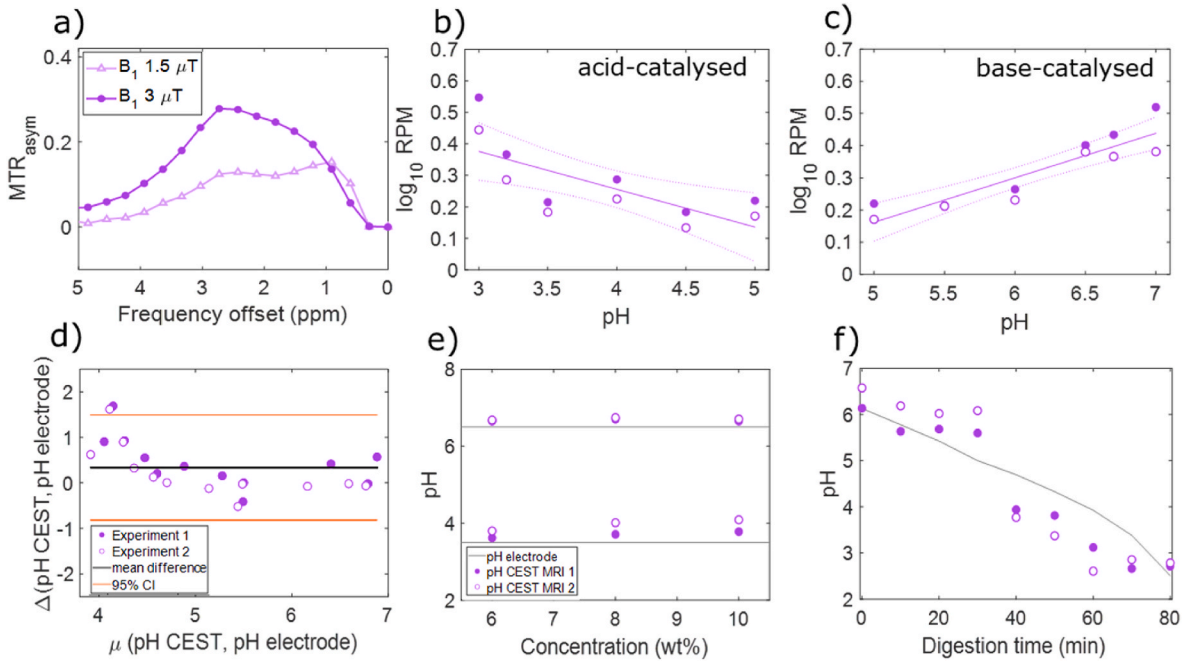

Fig. 3. Validation of CEST for pH estimation on a 7 T NMR spectrometer using 12% (wt%) WPIS. (a) MTR_{asym} curves at pH 6 obtained with a B_1 amplitude of 1.5 and 3 μT. The filled and empty symbols in b-f represent repeats of the same experiment. pH calibration lines for (b) acid- ($log_{10}\,RPM = -0.21 \cdot pH + 1.4; R^2 = 0.78$) and (c) base- ($log_{10}\,RPM = 0.25 \cdot pH - 0.9; R^2 = 0.94$) catalysed chemical exchange. The solid and dotted lines represent the linear fit and the 95% confidence bounds of the fit, respectively. The pooled SD was 0.05 for both the acid- and base-catalysed calibration lines. (d) Bland-Altman plot of the pH estimated by CEST MRI vs. the pH measured with an electrode for a set of validation samples with a pooled SD of 0.15. (e) pH at different concentrations showing stable pH estimates upon varying concentrations with a pooled SD of 0.1. (f) pH of the gastric content samples estimated by CEST MRI and measured by the pH electrode. The pooled SD of the pH estimated by CEST MRI was 0.3.

(Fig. 3a), and were used to calculate the RPM values of amines to construct the acid- (Fig. 3b) and base-catalysed (Fig. 3c) chemical exchange calibration lines. The ^{1}H chemical exchange between amines and water can occur through both acid-, base-, and auto-catalysis, leading to a pH-dependent "v-shaped" pattern of the chemical exchange, as described before (Bai et al., 1993; Liepinsh & Otting, 1996), but it is predominantly base-catalysed at pH > 5, and increasing exchange rates have been observed with increasing pH for amine ^{1}H in amino acids (Liepinsh & Otting, 1996; Wermter et al., 2022). The *RPM* value for the base-catalysed region showed a good linear correlation with pH (R^2 = 0.94), while the correlation for the acid-catalysed region was lower (R^2 = 0.78). This is likely due to the slower chemical exchange at low pH for amines, resulting in low measured MTR_{asym} values, especially at B_1 = 1.5 μT. Consequently, the CEST MRI approach is less sensitive at low pH values.

The calibration lines were used to estimate the pH of a set of validation samples of 12% WPIS ranging from pH 3–7. A Bland-Altman plot was used to assess the agreement between the pH values estimated by CEST MRI and those measured with a pH electrode (Fig. 3d). The mean difference was 0.34, which indicates a systematically higher pH estimated by the CEST MRI approach. The individual data points are scattered around the mean difference line, and are within the limits of agreement (LoA) except for the measurements around pH 4.2. The difference appears to increase at lower pH values, indicating an overestimation of the pH in the lower pH range (<4.5), which may be attributed to the lower sensitivity of CEST at low pH as explained above. Overall, there was a good agreement between the pH estimated by CEST MRI and the pH values measured with an electrode within the pH range of 4.5–7 (*NMRSD* = 0.04). The 95% CI for the pH estimated (Table S1) by the acid-catalysed calibration line (pH 3–5) was ±0.4 pH units, whereas that for the pH estimated by the base-catalysed calibration line was much smaller (±0.05 pH). Consequently, the pH range within which the CEST MRI approach allows for both accurate and precise pH estimates is pH 5–7. To assess whether the pH estimation is independent of protein concentration, we measured 6%, 8%, and 10% (wt%) WPI samples at pH 3.5 and 6.5. The obtained pH values were accurate and independent of protein concentration, as depicted in Fig. 3e. Subsequently, we used the calibration lines to estimate the pH of gastric content samples from the semi-dynamic digestion of 12% WPIS (Fig. 3f). The estimated pH values followed the same trend as the pH values measured by an electrode (grey line). However, the agreement between the two methods was lower (NMRSD = 0.14) compared to the data of the validation samples. Larger deviations were observed at later digestion times, consistently with previous observations for the validation samples at low pH. Based on these findings, we established that the pH range where CEST MRI can provide relatively accurate pH estimates is from 5 to 7; this can potentially aid *in vivo* mapping of the pH distribution throughout the stomach and determining the activation time of pepsin occurring at ~ pH 5.5 (Gray et al., 2014).

3.2.2. *Proof-of-concept in situ pH mapping during gastric digestion*

To further evaluate the feasibility of CEST MRI for *in vivo* pH mapping, CEST measurements were conducted on a 3 T clinical MRI scanner at 37 °C. The 12% WPIS at varying pH were measured to construct calibration curves for the acid- and base-catalysed chemical exchange (respectively, R^2 = 0.77 and R^2 = 0.74) (Fig. S2). It is worth noting that the R^2-value for the base-catalysed calibration line is lower at 3 T compared to that at 7 T.

This can be attributed to a shift in the chemical exchange peak observed in the CEST spectrum from Δ = 2.7 ppm at pH 3–6.5 to Δ = 3.5 ppm at pH ≥ 6.5 (Fig. S3). This leads to lower MTR_{asym} and RPM values at Δ = 2.7 ppm for pH 6.5–7. This shift in the Δ is most likely caused by the higher temperature (37 °C) used for the 3 T measurements, resulting in a downfield shift of the chemical shift of amine protons. For comparison, CEST spectra of 12% WPIS at pH 4, 5.5 and 7 were also measured on a 7 T MRI scanner at 37 °C, and a similar shift was observed

in the chemical exchange peak at pH 7 (Fig. S3).

The B_0-correction of the MTR_{asym} using the method introduced by Sun (2020), yielded results consistent with the standard WASSR approach (Fig. S4). The corrected maps were then used to generate *RPM* maps. The *RPM* per voxel was interpolated into the calibration lines to obtain a pH estimation per voxel as a function of the digestion time (Fig. 4a). Specifically, the calibration line for base- and acid-catalysed chemical exchange was used for the time periods t = 0–20 min and 30–60 min, respectively.

The pH maps for t = 0–20 min were homogeneous, which is in line with the homogeneous gastric content observed in the corresponding photographs of the gastric compartment (Fig. 4a). Additionally, the pH values estimated by CEST MRI were in close agreement with the mean pH measured by a pH electrode at 9 locations inside the beaker (Fig. 4b). After t = 30 min, the pH map becomes heterogeneous, consistent with visual observation of protein precipitation near the pI from t = 30 min onwards, as depicted in the photographs (Fig. 4a). Consequently, voxels containing these aggregates have lower MTR_{asym} values, due to the reduced accessibility of chemically-exchangeable protons. This ultimately leads to lower *RPM* values, resulting in an overestimation of the pH by the acid-catalysed chemical exchange calibration line. This is also apparent in Fig. 4b, where the mean pH estimated by CEST MRI at t > 30 min is higher than the pH measured by the electrode. Therefore, this approach allows accurate estimation of pH up to the pI of the proteins under study and it is sensitive to the aggregation phenomena occurring near the pI. Notably, the CEST MRI method holds potential for detecting the formation of small aggregates during gastric digestion that cannot be detected in T_2-weighted MRI images (Fig. S5). Whereas most applications of pH mapping using CEST MRI focus solely on a narrow pH range, typically pH 6–7 (Boyd et al., 2022; Chen et al., 2017; Tang et al., 2020), our findings demonstrate that for WPIS the method can cover a broader pH range from pH 5–7. This is a relevant range for gastric digestion of proteins, and therefore this approach is worth pursuing in vivo MRI studies.

We note that, for data collected on clinical MRI scanners, correction for B_1-inhomogeneity is crucial for reliable pH quantification. Here, we used the DREAM method for mapping the B_1, and used this for voxel-wise correction of the MTR_{asym} values using the two-point correction method (Windschuh et al., 2015). We selected the DREAM method because it allows rapid acquisition of a B_1-map, and is known to introduce smaller errors in the obtained B_1-values compared to other B_1-mapping methods, especially at low signal to noise ratios (SNR) (Gavazzi et al., 2019). These two advantages are especially important for our application, where SNR is sacrificed to achieve short measurement durations. We also acknowledge that Gavazzi et al. (2019) reported a relatively high bias of 6.2% and 15% for, respectively, the inner and outer tube of a phantom at 3 T. Such inaccuracies in the determined B_1-values can translate into inaccuracies in the B_1-corrected MTR_{asym} values and, subsequently, in the estimated pH. To assess this effect, we added a 15% bias to the B_1-map measured with the DREAM method on our 3 T scanner for the examined digestion times. We found that this resulted in a relatively large bias of ~13% in the B_1-corrected MTR_{asym} values. However, the corresponding effect on the pH was much smaller (0.82%). This is because the *RPM* parameter, used for estimating the pH, is more robust to inaccuracies in B_1 as compared to the MTR_{asym} parameter.

Moreover, we note that exchange regime depends on the strength of the magnetic field. For instance, at higher magnetic field strengths, the chemical shift (CS) difference between the two pools increases. This leads to a large CS difference with respect to the exchange rate ($k_{ex} \ll \Delta CS$), resulting in a slow exchange regime (Kleckner & Foster, 2011). Consequently the sensitivity and specificity of the method could be enhanced by utilizing a 7 T clinical MRI scanner. At this higher field strength we observed 1.5–2x higher MTR_{asym} values, depending on the pH and B_1 amplitude (Fig. S6). Additionally, a better separation between the exchange peak and water could be obtained (Fig. S3).

3.3. Quantitative assessment of MP coagulation at 3 T

In our previous work, we successfully applied T_2-weighted and MT

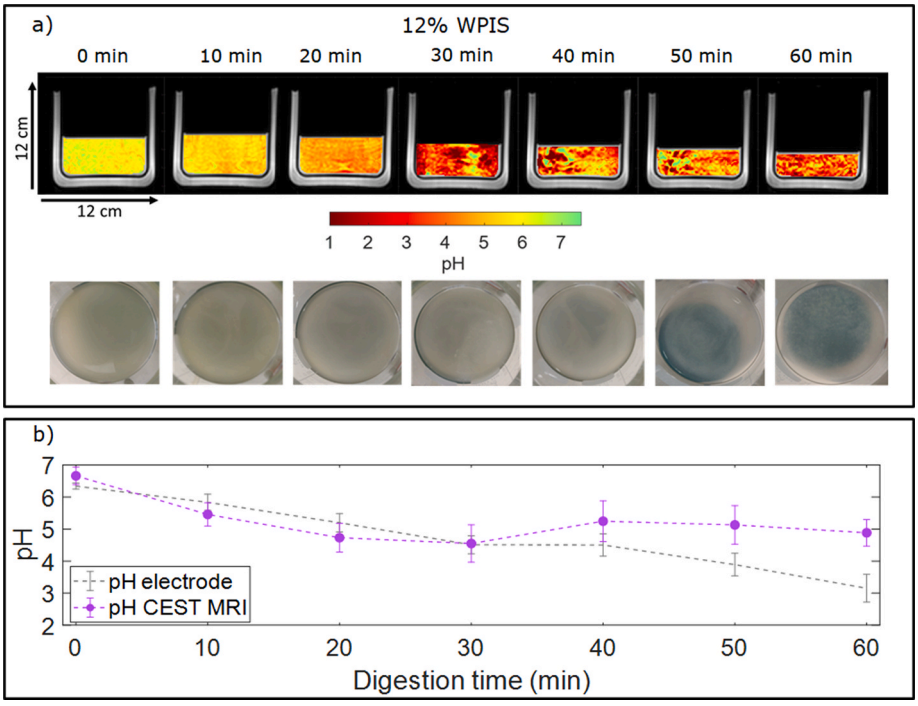

Fig. 4. (a) pH maps during semi-dynamic *in vitro* gastric digestion of 12% WPI obtained using the dual power CEST MRI approach on a 3 T clinical MRI scanner (top) and photographs of the beaker content during digestion (bottom). (c) Mean estimated pH of the gastric content (purple circles) and the mean pH measured by an electrode at 9 locations across the beaker content (grey line). The error bars for pH CEST MRI correspond to the SD of the pH across all the voxels (n = 2058–3248) in the gastric content. The error bars for pH electrode correspond to the standard deviation of the pH measured at 9 different locations across the beaker.

MRI to monitor MP coagulation in static *in vitro* digestion samples using a 7 T NMR spectrometer (Mayar et al., 2023). In the present study, we set out to assess the feasibility of using these methods for *in situ* assessment of MP coagulation and breakdown under semi-dynamic conditions on a 3 T clinical MRI scanner.

3.3.1. T_2-weighted MRI of MP coagulation and breakdown

Phase separation between high- and low-intensity voxels in the T_2-weighted images, as a result of gastric MP coagulation was observed from t = 10 min and 20 min onwards for LPSM and HPSM, respectively (Fig. 5a). The high-intensity voxels correspond to the liquid phase consisting of SGF and dissolved proteins and peptides, having long T_2-values. The low-intensity MRI voxels correspond to the coagulum phase within which water protons undergo rapid T_2 relaxation due to self-diffusional averaging and chemical exchange with immobile proteins. We note that the protons covalently bound to coagulated proteins have sub-ms T_2-values and, thus, are invisible in the conventional MRI measurements performed here.

For LPSM, the coagulum was visible in the T_2-weighted images until the last digestion time measured, while for HPSM it was nearly completely solubilized or the soft coagulated proteins were removed by gastric emptying after t = 50 min. It should be noted that, in some MRI slices other than the presented MRI slice of the gastric beaker, coagulated proteins were observed at t > 50 min. The measurements were conducted until t = 80 min, but here we only show the images up until t = 70 min because, for HPSM, the volume of gastric content was too low for visualization and quantification at t > 70 min.

The changes in the coagulum volume, estimated from the T_2-weighted images, varied as a function of the digestion time (Fig. 5b). The largest coagulum volume was observed at t = 10 min and 20 min for LPSM and HPSM, respectively. Subsequently, the coagulum volume decreased for both milk products, with a consistently higher volume observed for LPSM at t ≥ 30 min. While, the T_2-weighted images proved useful for both visualizing and quantifying the changes in the coagulum volume, they do not provide information on the structure of the coagulum. For that purpose, MT measurements were used as a complementary method.

3.3.2. MT MRI of MP coagulation

MTR maps of the coagulum (Fig. 6a) were obtained by applying the coagulum mask obtained from the T_2-weighted images to the MT data of the gastric beaker content. As digestion progressed, the *MTR* value within the coagulum increased, and a notable difference in the *MTR* maps of LPSM and HPSM was observed. The coagulum exhibited a greater spatial variability in the *MTR* values at later digestion time points, with the *MTR* maps of HPSM appearing more heterogeneous. The *MTR* values on the surface of the coagulum are lower, which might be due to partial-volume effects, and appear as a black/red edge.

The *MTR* distribution within the *MTR* maps (Fig. 6a) was unimodal and symmetric for both LPSM and HPSM at t = 0–10 min, indicating that the gastric content is described by one predominant *MTR* value, uniformly distributed across the gastric content. However, for later digestion times (t ≥ 20 min), the *MTR* distribution within the coagulum for LPSM and HPSM began to differ. For LPSM the distribution shifted to higher *MTR* values, became broader, bi-modal and less symmetrical around each peak, while a broadened unimodal symmetric distribution was observed for HPSM. For LPSM the mean *MTR* in the coagulum increased by 55% from t = 0–70 min. For HPSM, the *MTR* increased by 24% from t = 20–40 min followed by a continuous decrease until 70 min. An increase in the *MTR* can be attributed to variations in the macromolecular content and mobility, and in the magnetization transfer dynamics (Henkelman et al., 2001). We have previously shown that the *MTR* depends on the composite parameter $R_{ex}M_0^{ss}/R_1^w$, which includes the rate of magnetization transfer (R_{ex}), the population of semi-solid protons (M_0^{ss}) and the longitudinal relaxation rate of water (R_1^w) (Mayar et al., 2022). In our previous work, we observed that the R_1^w did

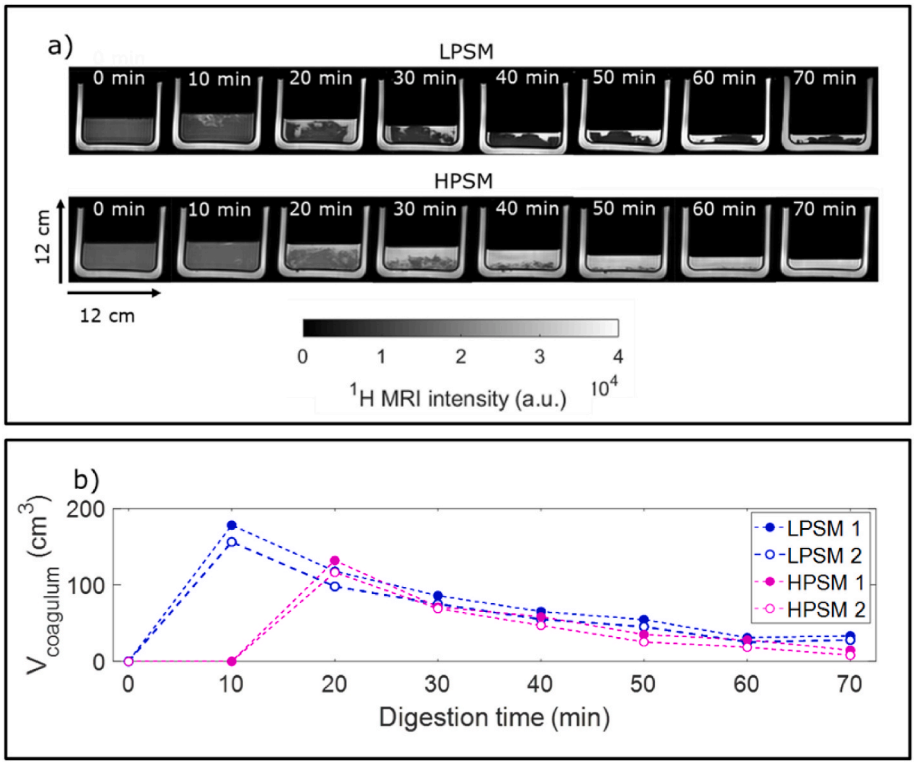

Fig. 5. (a) T_2-weighted MRI images of LPSM and HPSM during semi-dynamic *in vitro* gastric digestion measured on a 3 T clinical MRI scanner. (b) Coagulum volume as a function of the digestion time obtained by intensity thresholding of the T_2-weighted images. The filled and empty symbols represent repeats of the same experiment. The pooled SD was 9 and 6, respectively, for LPSM and HPSM.

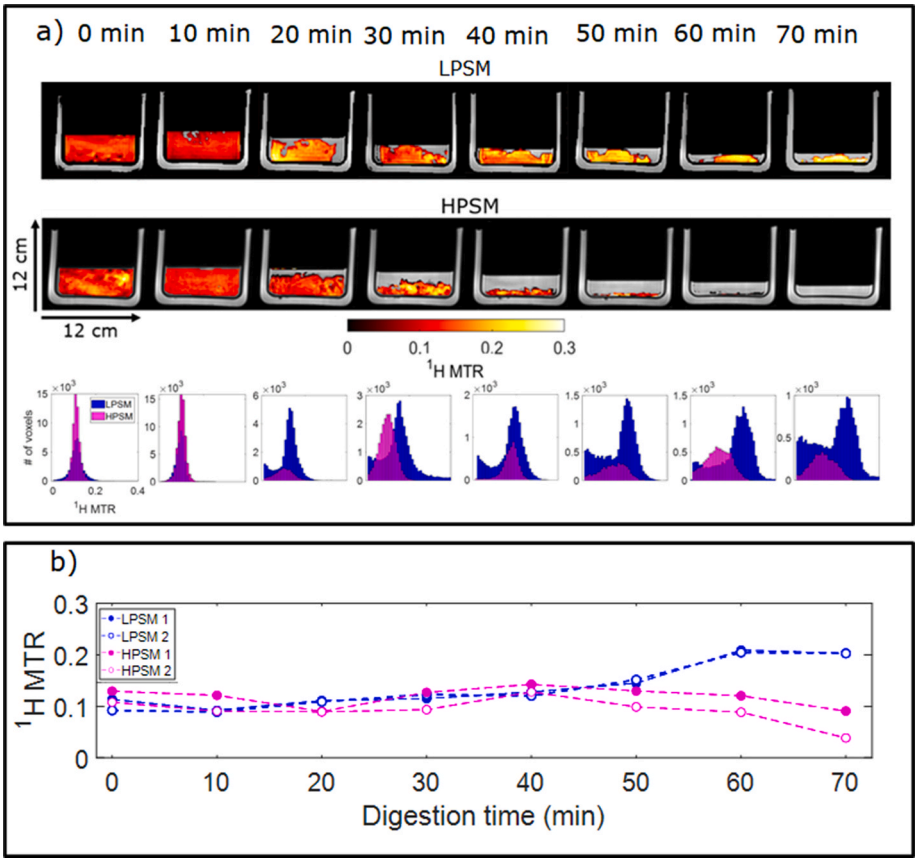

Fig. 6. (a) ^{1}H MTR MRI maps of the coagulum for LPSM and HPSM during semi-dynamic *in vitro* gastric digestion measured on a 3 T clinical MRI scanner (top) and histograms with a bin width of 0.01 of the *MTR* inside the coagulum (bottom). (c) Mean *MTR* of the coagulum voxels as a function the digestion time. The empty and filled symbols refer to repeats of the same experiment. The pooled SD was 0.01 and 0.02, respectively, for LPSM and HPSM.

not change during *in vitro* digestion. Therefore, the increased *MTR* observed for the MP coagulum during gastric digestion could be the result of a decrease in macromolecular mobility and an increase in the protein content within the coagulum. Constrained macromolecular mobility results in stronger inter- and intra-molecular dipolar interactions, which are the drivers of magnetization transfer (van Zijl et al., 2018). This increase in dipolar interactions yields greater efficiency in magnetization transfer between the two proton pools and, hence, a higher *MTR*.

To better understand the increase in the *MTR* of the coagulum, *G*' and *G*" of the LPSM coagulum at t = 20, 40 and 70 min were measured (Fig. S7). The *G*' and *G*" values at t = 20 and 40 min are similar. However, a clear increase in both parameters was observed from t = 40 up to 70 min. This observation is in line with the *MTR* data, where little variation was observed between t = 20 and 40 min, followed by an increase up to t = 70 min. The *G*' represents the ability of a material to store and recover elastic energy, and can be used to quantify its resistance to deformation. On the other hand, the *G*" represents the viscous component of a material's response to cyclic deformation and can be used to quantify a material's ability to dissipate energy and flow or deform plastically (Macosko, 1996). These observations are consistent with previous studies that demonstrated an increase in the *G*' and *G*" during acid and rennet coagulation of milk (Le Feunteun et al., 2012; Le Feunteun & Mariette, 2008). Moreover, Roy et al. (2022) showed an increase in the complex modulus (G^*), a parameter that describes the complete viscoelastic behaviour of a material by combining the *G*' and *G*", during *in vivo* gastric digestion of raw cow's milk in piglets. Both the increase in *G*' and *G*'' point to a protein network that is becoming more dense and non-covalently crosslinked. The concomitant decrease in molecular mobility and increase in dipolar interactions within the protein network is reflected by the increase in the *MTR*. We note that the variability in the rheology data is large due to the inherent heterogeneity of the coagulum.

CLSM was used to assess changes in the coagulum at the micron-scale (Fig. S8). For both LPSM and HPSM, at t = 20 min the micron-scale protein network within the coagulum appeared to be porous with void spaces filled with liquid entrapped within the protein network. The coagulum appeared more compact as digestion progressed, and minimal variation was observed in the microstructure of the coagulum between 40 and 70 min. Overall, both the CLSM and rheology data indicate that changes in protein network density and mobility within the coagulum are reflected in the *MTR* values.

Overall, these results demonstrate that CEST and MT combined with T_2-weighted imaging can be used to probe pH and MP coagulation under semi-dynamic *in vitro* gastric digestion conditions. This integrated approach may offer a more comprehensive overview of gastric digestion compared to the use of only T_2-weighted imaging for measuring GE and visual assessment of phase separation or coagulation. The measurements presented here are fast enough to be feasible for monitoring gastric digestion over time in *vivo* human studies. The primary challenge of *in vivo* measurements is the presence of motion due to breathing and peristaltic contractions of the stomach. Breathing-related motion artifacts can be minimized by performing each scan within one breath-hold, which is common practice in clinical MRI of the abdominal area. Furthermore, motion-induced artifacts in the calculated *MTR* and MTR_{asym} maps can be reduced through image registration of the S_0 and S_{sat} images. In this study, our primary focus was gastric digestion, as it is the first step in MP digestion. Gastric digestion involves structuring and de-structuring of milk to facilitate further breakdown of MPs in the intestines. Consequently, gastric digestion may influence intestinal

digestion, thereby affecting absorption of amino acids in the bloodstream. In future works, it would be interesting to link gastric digestion to the absorption of amino acids in the bloodstream.

4. Conclusions

In this work, we explored the use of CEST and MT MRI for monitoring pH and MP coagulation during semi-dynamic *in vitro* gastric digestion using 12% WPIS, LPSM and HPSM as test products. Our results demonstrate that the MTR_{asym} can be used to monitor concomitant pH and protein concentration changes during gastric digestion, and is sensitive to the effect of heat treatment on these changes. The dual-power CEST method was successfully validated on a 7 T NMR spectrometer as an indirect method for measuring pH using the 12% WPIS. The method enabled accurate determination of the pH in the range of 5–7. Accurate *in situ* pH mapping was also achieved on a 3 T clinical MRI scanner until t = 20 min of digestion, but heterogeneities and inaccuracies in the estimated pH arose from 30 min onwards due to protein aggregation near the pI. Moreover, a combination of T_2-weighted images and *MTR* maps obtained *in situ* during semi-dynamic digestion on a 3 T clinical MRI scanner, proved to be valuable for assessing changes in coagulum volume and consistency, and for revealing differences in gastric coagulation behaviour between differently heated milk products.

In summary, our findings demonstrate that the combined use of CEST, MT, and T_2-weighted MRI can be used to effectively capture the variations in pH and coagulation dynamics, allowing for the investigation of the impact of different heat treatments on gastric MP digestion. These findings are a significant advancement towards future assessment of *in vivo* gastric MP digestion in humans using MRI.

Source of funding

This work was part of a public-private partnership supported by the Dutch Ministry of Economic Affairs Top Sector Agri&Food (grant number AF-18012).

CRediT authorship contribution statement

Morwarid Mayar: Conceptualization, Data curation, Formal analysis, Investigation, Methodology, Validation, Visualization, Writing – original draft. **Mart de Vries:** Formal analysis, Investigation, Methodology, Writing – review & editing. **Paul Smeets:** Conceptualization, Methodology, Supervision, Validation, Writing – review & editing. **John van Duynhoven:** Conceptualization, Methodology, Validation, Writing – review & editing, Supervision. **Camilla Terenzi:** Conceptualization, Methodology, Supervision, Validation, Writing – review & editing.

Declaration of competing interest

The authors declare the following financial interests/personal relationships which may be considered as potential competing interests:

John van Duynhoven has an employment with a company (Unilever) that uses dairy ingredients to manufacture food products. The other authors declare that they have no competing financial interests or personal relationships that could have appeared to influence the work reported in this paper.

Data availability

Data will be made available on request.

Acknowledgements

Lucas van Grootveld is gratefully acknowledged for performing the CEST measurement of LPSM on the 7 T NMR spectrometer. We also acknowledge the MAGNEFY centre which was supported by the uNMR-NL Grid: A distributed, state-of-the-art Magnetic Resonance facility for the Netherlands (NWO grant 184.035.002). John Philippi is thanked for expert technical support on the 7 T NMR spectrometer. The use of the 3 T MRI facility has been made possible by Wageningen University & Research Shared Research Facilities. Paul de Bruin is thanked for his expert support with setting up the measurements on the 3 T clinical MRI scanner. Jeanine Prompers and Hans Hoogduin are thanked for their help with the measurements on the 7 T clinical MRI scanner. Arjen Bader is thanked for his help with the CLSM measurements. Raoul Fix is thanked for his help with the rheology measurements.

Appendix A. Supplementary data

Supplementary data to this article can be found online at https://doi.org/10.1016/j.foodhyd.2024.109866.

References

Bai, Y., Milne, J. S., Mayne, L., & Englander, S. W. (1993). Primary structure effects on peptide group hydrogen exchange. *Proteins: Structure, Function, and Genetics, 17*(1), 75–86. https://doi.org/10.1002/prot.340170110

Balaban, R. S., & Ceckler, T. (1992). Magnetization transfer contrast in magnetic resonance imaging. *Magnetic Resonance Quarterly, 8*(2), 116–137.

Bornhorst, G. M., & Paul Singh, R. (2014). Gastric digestion in vivo and in vitro: How the structural Aspects of food influence the digestion process. *Annual Review of Food Science and Technology, 5*(1), 111–132. https://doi.org/10.1146/annurev-food-030713-092346

Boyd, P. S., Breitling, J., Korzowski, A., Zaiss, M., Franke, V. L., Mueller-Decker, K., Glinka, A., Ladd, M. E., Bachert, P., & Goerke, S. (2022). Mapping intracellular pH in tumors using amide and guanidyl CEST-MRI at 9.4 T. *Magnetic Resonance in Medicine, 87*(5), 2436–2452. https://doi.org/10.1002/mrm.29133

Brodkorb, A., Egger, L., Alminger, M., Alvito, P., Assunção, R., Ballance, S., Bohn, T., Bourlieu-Lacanal, C., Boutrou, R., Carrière, F., Clemente, A., Corredig, M., Dupont, D., Dufour, C., Edwards, C., Golding, M., Karakaya, S., Kirkhus, B., Le Feunteun, S., … Recio, I. (2019). INFOGEST static in vitro simulation of gastrointestinal food digestion. *Nature Protocols, 14*(4), 991–1014. https://doi.org/10.1038/s41596-018-0119-1

Carver, J. P., & Richards, R. E. (1972). A general two-site solution for the chemical exchange produced dependence of T2 upon the carr-Purcell pulse separation. *Journal of Magnetic Resonance, 6*(1), 89–105. https://doi.org/10.1016/0022-2364(72)90090-X, 1969.

Chen, M., Chen, C., Shen, Z., Zhang, X., Chen, Y., Lin, F., Ma, X., Zhuang, C., Mao, Y., Gan, H., Chen, P., Zong, X., & Wu, R. (2017). Extracellular pH is a biomarker enabling detection of breast cancer and liver cancer using CEST MRI. *Oncotarget, 8*(28), 45759–45767. https://doi.org/10.18632/oncotarget.17404

Deng, R., Janssen, A. E. M., Vergeldt, F. J., Van As, H., de Graaf, C., Mars, M., & Smeets, P. A. M. (2020). Exploring in vitro gastric digestion of whey protein by time-domain nuclear magnetic resonance and magnetic resonance imaging. *Food Hydrocolloids, 99*(August 2019), Article 105348. https://doi.org/10.1016/j.foodhyd.2019.105348

Deng, R., Mars, M., Janssen, A. E. M., & Smeets, P. A. M. (2023). Gastric digestion of whey protein gels: A randomized cross-over trial with the use of MRI. *Food Hydrocolloids*. , Article 108689. https://doi.org/10.1016/j.foodhyd.2023.108689

Deng, R., Seimys, A., Mars, M., Janssen, A. E. M., & Smeets, P. A. M. (2022). Monitoring pH and whey protein digestion by TD-NMR and MRI in a novel semi-dynamic in vitro gastric simulator (MR-GAS). *Food Hydrocolloids, 125*, Article 107393. https://doi.org/10.1016/j.foodhyd.2021.107393

Dupont, D., & Mackie, A. R. (2015). Static and dynamic in vitro digestion models to study protein stability in the gastrointestinal tract. *Drug Discovery Today: Disease Models, 17–18*, 23–27. https://doi.org/10.1016/j.ddmod.2016.06.002

Gavazzi, S., van den Berg, C. A. T., Sbrizzi, A., Kok, H. P., Stalpers, L. J. A., Lagendijk, J. J. W., Crezee, H., & van Lier, A. L. H. M. W. (2019). Accuracy and precision of electrical permittivity mapping at 3T: The impact of three mapping techniques. *Magnetic Resonance in Medicine, 81*(6), 3628–3642. https://doi.org/10.1002/mrm.27675

Gottwald, A., Creamer, L. K., Hubbard, P. L., & Callaghan, P. T. (2005). Diffusion, relaxation, and chemical exchange in casein gels: A nuclear magnetic resonance study. *The Journal of Chemical Physics, 122*(3). https://doi.org/10.1063/1.1825383

Gray, V. A., Marques, C., M, R., Cole, E., Riva Toma, J. M. D., Ghidorsi, L., … Eranui, T. (2014). Use of enzymes in the dissolution testing of gelatin capsules and gelatin-coated tablets-revisions to dissolution <711> and disintegration and dissolution of dietary supplements <2040>. *Dissolution Technologies, 21*(4), 6–18. https://doi.org/10.14227/DT210414P6

Henkelman, R. M., Stanisz, G. J., & Graham, S. J. (2001). Magnetization transfer in MRI: A review. *NMR in Biomedicine, 14*(2), 57–64. https://doi.org/10.1002/nbm.683

Hills, B. P., Takacs, S. F., & Belton, P. S. (1989). The effects of proteins on the proton N.M.R. transverse relaxation times of water. *Molecular Physics, 67*(4), 903–918. https://doi.org/10.1080/00268978900101531

Hills, B. P., Takacs, S. F., & Belton, P. S. (1990). A new interpretation of proton NMR relaxation time measurements of water in food. *Food Chemistry, 37*(2), 95–111. https://doi.org/10.1016/0308-8146(90)90084-H

Hinrichs, R., Bulca, S., & Kulozik, U. (2007). Water mobility during renneting and acid coagulation of casein solutions: A differentiated low-resolution nuclear magnetic resonance analysis. *International Journal of Dairy Technology, 60*(1), 37–43. https://doi.org/10.1111/j.1471-0307.2007.00290.x

Huppertz, T., & Chia, L. W. (2021). Milk protein coagulation under gastric conditions: A review. *International Dairy Journal, 113*, Article 104882. https://doi.org/10.1016/j.idairyj.2020.104882

Kim, M., Gillen, J., Landman, B. A., Zhou, J., & Van Zijl, P. C. M. (2009). Water saturation shift referencing (WASSR) for chemical exchange saturation transfer (CEST) experiments. *Magnetic Resonance in Medicine, 61*(6), 1441–1450. https://doi.org/10.1002/mrm.21873

Kleckner, I. R., & Foster, M. P. (2011). An introduction to NMR-based approaches for measuring protein dynamics. *Biochimica et Biophysica Acta (BBA) - Proteins and Proteomics, 1814*(8), 942–968. https://doi.org/10.1016/j.bbapap.2010.10.012

Le Feunteun, S., & Mariette, F. (2008). Effects of acidification with and without rennet on a concentrated casein system: A kinetic NMR probe diffusion study. *Macromolecules, 41*(6), 2079–2086. https://doi.org/10.1021/ma702248z

Le Feunteun, S., Ouethrani, M., & Mariette, F. (2012). The rennet coagulation mechanisms of a concentrated casein suspension as observed by PFG-NMR diffusion measurements. *Food Hydrocolloids, 27*(2), 456–463. https://doi.org/10.1016/j.foodhyd.2011.09.008

Liepinsh, E., & Otting, G. (1996). Proton exchange rates from amino acid side chains—implications for image contrast. *Magnetic Resonance in Medicine, 35*(1), 30–42. https://doi.org/10.1002/mrm.1910350106

Longo, D. L., Sun, P. Z., Consolino, L., Michelotti, F. C., Uggeri, F., & Aime, S. (2014). A general MRI-CEST ratiometric approach for pH imaging: Demonstration of in vivo pH mapping with iobitridol. *Journal of the American Chemical Society, 136*(41), 14333–14336. https://doi.org/10.1021/ja5059313

Mackie, A., Mulet-Cabero, A.-I., & Torcello-Gómez, A. (2020). Simulating human digestion: Developing our knowledge to create healthier and more sustainable foods. *Food & Function, 11*(11), 9397–9431. https://doi.org/10.1039/D0FO01981J

Macosko, C. W. (1996). *Rheology: Principles, measurements, and applications* (1st ed.). Wiley-VCH.

Mayar, M., Miltenburg, J. L., Hettinga, K., Smeets, P. A. M., van Duynhoven, J. P. M., & Terenzi, C. (2022). Non-invasive monitoring of in vitro gastric milk protein digestion kinetics by 1H NMR magnetization transfer. *Food Chemistry, 383*(February), Article 132545. https://doi.org/10.1016/j.foodchem.2022.132545

Mayar, M., Smeets, P., Duynhoven, J., & Terenzi, C. (2023). In vitro 1H MT and CEST MRI mapping of gastro-intestinal milk protein breakdown. *Food Structure, 36*, 100314–100324.

Ménard, O., Bourlieu, C., De Oliveira, S. C., Dellarosa, N., Laghi, L., Carrière, F., Capozzi, F., Dupont, D., & Deglaire, A. (2018). A first step towards a consensus static in vitro model for simulating full-term infant digestion. *Food Chemistry, 240*, 338–345. https://doi.org/10.1016/j.foodchem.2017.07.145, 2017.

Mulet-Cabero, A. I., Egger, L., Portmann, R., Ménard, O., Marze, S., Minekus, M., Le Feunteun, S., Sarkar, A., Grundy, M. M. L., Carrière, F., Golding, M., Dupont, D., Recio, I., Brodkorb, A., & Mackie, A. (2020). A standardised semi-dynamic: In vitro digestion method suitable for food-an international consensus. *Food & Function, 11*(2), 1702–1720. https://doi.org/10.1039/c9fo01293a

Mulet-Cabero, A. I., Mackie, A. R., Wilde, P. J., Fenelon, M. A., & Brodkorb, A. (2019). Structural mechanism and kinetics of in vitro gastric digestion are affected by process-induced changes in bovine milk. *Food Hydrocolloids, 86*, 172–183. https://doi.org/10.1016/j.foodhyd.2018.03.035

Musse, M., Le Feunteun, S., Collewet, G., Ravilly, M., Quellec, S., Ossemond, J., Morzel, M., Challois, S., Nau, F., & Lucas, T. (2023). Quantitative magnetic resonance imaging of in vitro gastrointestinal digestion of a bread and cheese meal. *Food Research International, 169*, 112821–112833.

Nehrke, K., & Börnert, P. (2012). DREAM—a novel approach for robust, ultrafast, multislice B1 mapping. *Magnetic Resonance in Medicine, 68*(5), 1517–1526. https://doi.org/10.1002/MRM.24158

Nicolai, T., Britten, M., & Schmitt, C. (2011). β-Lactoglobulin and WPI aggregates Formation, structure and applications. *Food Hydrocolloids, 25*, 1945–1962.

Pederson, J. B., Fojan, P., Sorensen, J., & Petersen, S. B. (2006). Towards control of aggregational behaviour of α-lactalbumin at acidic pH. *Journal of Fluorescence, 16*, 611–621.

Roy, D., Moughan, P. J., Ye, A., Hodgkinson, S. M., Stroebinger, N., Li, S., Dave, A. C., Montoya, C. A., & Singh, H. (2022). Structural changes in milk from different species during gastric digestion in piglets. *Journal of Dairy Science, 105*(5), 3810–3831. https://doi.org/10.3168/jds.2021-21388

Smeets, P. A. M., Deng, R., Van Eijnatten, E. J. M., & Mayar, M. (2020). Monitoring food digestion with magnetic resonance techniques. *Proceedings of the Nutrition Society, 3*, 1–11. https://doi.org/10.1017/S0029665120007867

Spiller, R., & Marciani, L. (2019). Intraluminal impact of food: New insights from MRI. *Nutrients, 11*(5), 1147–1161. https://doi.org/10.3390/nu11051147

Sun, P. Z. (2020). Fast correction of B0 field inhomogeneity for pH-specific magnetization transfer and relaxation normalized amide proton transfer imaging of acute ischemic stroke without Z-spectrum. *Magnetic Resonance in Medicine, 83*(5), 1688–1697. https://doi.org/10.1002/mrm.28040

Tang, Y., Xiao, G., Shen, Z., Zhuang, C., Xie, Y., Zhang, X., Yang, Z., Guan, J., Shen, Y., Chen, Y., Lai, L., Chen, Y., Chen, S., Dai, Z., Wang, R., & Wu, R. (2020). Noninvasive detection of extracellular pH in human benign and malignant liver tumors using CEST MRI. *Frontiers in Oncology, 10*. https://doi.org/10.3389/fonc.2020.578985

Tome, D. (2012). Criteria and markers for protein quality assessment – a review. *British Journal of Nutrition, 108*(S2), S222–S229. https://doi.org/10.1017/S0007114512002565

Tunick, M. H., Ren, D. X., Van Hekken, D. L., Bonnaillie, L., Paul, M., Kwoczak, R., & Tomasula, P. M. (2016). Effect of heat and homogenization on in vitro digestion of milk. *Journal of Dairy Science, 99*(6), 4124–4139. https://doi.org/10.3168/jds.2015-10474

van Lieshout, G. A. A., Lambers, T. T., Bragt, M. C. E., & Hettinga, K. A. (2019). How processing may affect milk protein digestion and overall physiological outcomes: A systematic review. *Critical Reviews in Food Science and Nutrition, 0*(0), 1–24. https://doi.org/10.1080/10408398.2019.1646703

Van Obberghen, E., Mchinda, S., le Troter, A., Prevost, V. H., Viout, P., Guye, M., Varma, G., Alsop, D. C., Ranjeva, J.-P., Pelletier, J., Girard, O., & Duhamel, G. (2018). Evaluation of the sensitivity of inhomogeneous magnetization transfer (ihMT) MRI for multiple sclerosis. *American Journal of Neuroradiology, 39*(4), 634–641. https://doi.org/10.3174/ajnr.A5563

van Zijl, P. C. M., Lam, W. W., Xu, J., Knutsson, L., & Stanisz, G. J. (2018). Magnetization transfer contrast and chemical exchange saturation transfer MRI. Features and analysis of the field-dependent saturation spectrum. *NeuroImage, 168*, 222–241. https://doi.org/10.1016/j.neuroimage.2017.04.045

Wang, X., Ye, A., Lin, Q., Han, J., & Singh, H. (2018). Gastric digestion of milk protein ingredients: Study using an in vitro dynamic model. *Journal of Dairy Science, 101*(8), 6842–6852. https://doi.org/10.3168/jds.2017-14284

Ward, K. M., Aletras, A. H., & Balaban, R. S. (2000). A new class of contrast agents for MRI based on proton chemical exchange dependent saturation transfer (CEST). *Journal of Magnetic Resonance, 143*(1), 79–87. https://doi.org/10.1006/jmre.1999.1956

Weiger, M., & Pruessmann, K. P. (2019). Short-T2 MRI: Principles and recent advances. *Progress in Nuclear Magnetic Resonance Spectroscopy, 114*(115), 237–270. https://doi.org/10.1016/j.pnmrs.2019.07.001

Welsch, G. H., Trattnig, S., Scheffler, K., Szomonanyi, P., Quirbach, S., Marlovits, S., Domayer, S., Bieri, O., & Mamisch, T. C. (2008). Magnetization transfer contrast and T2 mapping in the evaluation of cartilage repair tissue with 3T MRI. *Journal of Magnetic Resonance Imaging, 28*(4), 979–986. https://doi.org/10.1002/jmri.21516

Wermter, F. C., Bock, C., & Dreher, W. (2022). Characterization of amine proton exchange for analyzing the specificity and intensity of the CEST effect: From humans to fish. *NMR in Biomedicine, 35*(2). https://doi.org/10.1002/nbm.4622

Windschuh, J., Zaiss, M., Meissner, J. E., Paech, D., Radbruch, A., Ladd, M. E., & Bachert, P. (2015). Correction of B1-inhomogeneities for relaxation-compensated CEST imaging at 7T. *NMR in Biomedicine, 28*(5), 529–537. https://doi.org/10.1002/nbm.3283

Wolff, S. D., & Balaban, R. S. (1989). Magnetization transfer contrast (MTC) and tissue water proton relaxationin vivo. *Magnetic Resonance in Medicine, 10*(1), 135–144. https://doi.org/10.1002/mrm.1910100113

Wu, B., Warnock, G., Zaiss, M., Lin, C., Chen, M., Zhou, Z., Mu, L., Nanz, D., Tuura, R., & Delso, G. (2016). An overview of CEST MRI for non-MR physicists. *EJNMMI Physics, 3*(1). https://doi.org/10.1186/s40658-016-0155-2

Wu, R., Longo, D. L., Aime, S., & Sun, P. Z. (2015). Quantitative description of radiofrequency (RF) power-based ratiometric chemical exchange saturation transfer (CEST) pH imaging. *NMR in Biomedicine, 28*(5), 555–565. https://doi.org/10.1002/nbm.3284

Ye, A., Weilin, L., Cui, J., Kong, Z., Roy, D., Kong, Y., Han, J., & Singh, H. (2019). Coagulation behaviour of milk under gastric digestion: Effect of pasteurization and ultra-high temperature treatment. *Food Chemistry, 286*, 216–225.

Zhou, Y., Bie, C., van Zijl, P. C. M., & Yadav, N. N. (2023). The relayed nuclear Overhauser effect in magnetization transfer and chemical exchange saturation transfer MRI. *NMR in Biomedicine, 36*(6). https://doi.org/10.1002/nbm.4778